




# Discerning Parallax Amplitude in Astrometric Microlensing

Sedighe Sajadian , Arya Mahmoudzadeh, and Setareh MoeinDepartment of Physics, Isfahan University of Technology, Isfahan 84156-83111, Iran; [s.sajadian@iut.ac.ir](mailto:s.sajadian@iut.ac.ir)

Received 2023 August 3; revised 2023 September 14; accepted 2023 September 28; published 2023 October 19

## Abstract

Gravitational microlensing is a powerful method for discovering isolated stellar-mass black holes (ISMBHs). These objects make long-duration microlensing events. To characterize these lensing objects by fully resolving the microlensing degeneracy, measurements of parallax and astrometric deflections are necessary. Microlensing events due to ISMBHs have considerable astrometric deflections but small parallax amplitudes,  $\pi_E \propto 1/\sqrt{M_1}$ , where  $M_1$  is the lens mass. We numerically investigate the possibility of inferring parallax amplitude from astrometric deflection in microlensing events due to ISMBHs. The parallax amplitude in astrometric deflections is proportional to the relative parallax  $\pi_{\text{rel}}$ , which means that it (i) does not strongly depend on  $M_1$  and (ii) increases in microlensing observations toward the Magellanic Clouds. We assume that these events will be potentially detected in upcoming microlensing surveys such as (1) the Roman observations of the Galactic bulge (GB) and (2) the LSST observations of the Large Magellanic Cloud (LMC) and that the Extremely Large Telescope (ELT) will follow up on them with one data point every 10 days. We evaluate the probability of inferring parallax amplitude from these observations by calculating the Fisher and covariance matrices. For the GB, the efficiencies for discerning parallax amplitudes with a relative error of  $<4\%$  through astrometric and photometric observations are 3.8% and 29.1%, respectively. For observations toward the LMC, these efficiencies are 41.1% and 23.0%, respectively. Measuring parallax amplitude through astrometric deflections is plausible in GB events with a lens distance of  $\lesssim 2.7$  kpc and in LMC halo lensing. By monitoring long-duration microlensing events, the ELT can detect astrometric deflections and their parallax-induced deviations.

*Unified Astronomy Thesaurus concepts:* Gravitational microlensing (672); Astrometric microlensing effect (2140); Annual microlensing parallax (2149); Monte Carlo methods (2238); Computational methods (1965)

## 1. Introduction


A short time after the famous paper by Paczynski (1986) concerning the detection of massive compact halo objects (MACHOs) in the Galactic halo through continuous observations toward the Magellanic Clouds (MCs), three microlensing groups, i.e., the Expérience de Recherche d'Objets Sombres (Aubourg et al. 1993), MACHO (Wu 1994), and the Optical Gravitational Lensing Experiment (Szymanski et al. 1994), searched for ongoing microlensing events. The first generation of microlensing surveys observed MCs for 10 yr to find the source stars that were being lensed by massive objects inside the Galactic halo. The most important result of these observations was the determination of an upper limit on the contribution of MACHOs in the Galactic halo (Alcock et al. 1998, 2000a; Lasserre et al. 2000). Since MACHOs have only gravitational interactions, studying and characterizing these objects is possible through gravitational microlensing observations.

The second generation of survey microlensing groups changed the observational direction from MCs to the Galactic bulge (GB) and spiral arms to discover extrasolar planets inside the Galactic disk and, additionally, probe the Galactic structure (Kiraga & Paczynski 1994; Albrow et al. 1996; EROS Collaboration et al. 1999; Alcock et al. 2000b; Udalski et al. 2000; Moniez et al. 2017). In planetary microlensing events, an extrasolar planet (exoplanet) is usually orbiting the lens object and makes a deviation in the magnification curve (see, e.g.,

Mao & Paczynski 1991; Gould & Loeb 1992). So far, more than 204 extrasolar planets have been confirmed in microlensing observations.<sup>1</sup> This population of exoplanets discovered by gravitational microlensing observations has the following special properties. (a) These exoplanets lie mostly beyond the snowline of their parent stars. (b) In microlensing events toward the GB, planetary lensing systems are typically found at radial distances of greater than 1000 pc from the observer. (c) These exoplanets are orbiting the host stars, which are usually very dim or dark (see, e.g., Gaudi 2012). Gravitational microlensing is therefore complementary to other methods for discovering extrasolar planets. In other methods (e.g., transits, radial velocimetry, astrometry), planetary systems must be close to the observer, and their host stars must be bright.

Applications of survey microlensing observations are not limited to the mentioned cases. For example, a new population of free-floating planets in the Galactic disk was discovered through densely observing the GB (Mróz et al. 2017; Sumi et al. 2023). Discovering isolated stellar-mass black holes (ISMBHs) inside the Galactic disk is another outstanding application of gravitational microlensing (Agol et al. 2002; Bennett et al. 2002; Mao et al. 2002; Lu et al. 2016; Lam et al. 2022; Sahu et al. 2022). Such isolated objects most likely do not emit X-ray emissions. Hence, they are only discernible through probing long-duration and achromatic amplifications in the light of background source stars.

Despite such vast and unique applications of gravitational microlensing, there is a problem when interpreting microlensing observations: degeneracy (see, e.g., Sajadian 2023). However, microlensing degeneracies can be resolved through

 Original content from this work may be used under the terms of the [Creative Commons Attribution 4.0 licence](https://creativecommons.org/licenses/by/4.0/). Any further distribution of this work must maintain attribution to the author(s) and the title of the work, journal citation and DOI.

<sup>1</sup> <https://exoplanetarchive.ipac.caltech.edu/>

measuring both (a) the parallax amplitude in the magnification factor (Gould 1994) and (b) the finite-source effect (Witt & Mao 1994). Instead of resolving the finite-source effect, measuring either lensing-induced astrometric deflection in the source trajectory (see, e.g., Hog et al. 1995; Miyamoto & Yoshii 1995; Walker 1995; Miralda-Escude 1996; Dominik & Sahu 2000) or the images' distance at the time of the closest approach (Dong et al. 2019; Zang et al. 2020), or resolving the source and lens and measuring proper motions with adaptive optics observations (Bhattacharya et al. 2018; Terry et al. 2022), will help to resolve the microlensing degeneracy. The parallax effect refers to the observer's motion around the Sun. This effect causes some periodic perturbations in the microlensing light curves (Gould 1994).

In long-duration microlensing events due to dark and massive lens objects (e.g., ISMBHs), this method for resolving microlensing degeneracy is somewhat challenging because the normalized parallax amplitude decreases as  $\pi_E \propto 1/\sqrt{M_1}$ , where  $M_1$  is the lens mass (see, e.g., Karolinski & Zhu 2020). However, the scale of the astrometric deflection in the source trajectory (i.e.,  $\theta_E$ , which is the angular Einstein radius) in these events is considerable because  $\theta_E \propto \sqrt{M_1}$ . In this work, we discuss the possibility of discerning parallax amplitudes in astrometric deflections of source trajectories. We show that parallax-induced perturbations in the astrometric deflection are directly proportional to the relative parallax  $\pi_{\text{rel}}$  and do not depend strongly on the lens mass. Hence, measuring the parallax amplitude is possible in the astrometric deflections of source trajectories in microlensing events toward MCs. However, microlensing events due to more massive lens objects are more suitable because they have considerable astrometric deflections in source trajectories.

The paper is organized as follows. In the first subsection of Section 2, we explain the formalism of astrometric microlensing events by including the parallax effect. Then, in Sections 2.2 and 2.3, by simulating astrometric microlensing events due to ISMBHs by considering the parallax effect toward the GB and Large Magellanic Cloud (LMC), respectively, we statistically evaluate parallax-induced deviations. In Section 3, we do realistic Monte Carlo simulations based on upcoming survey microlensing observations by the Roman (Spergel et al. 2015) and Vera C. Rubin Observatory's Legacy Survey of Space and Time (LSST; Ivezić et al. 2009) telescopes. We also consider potential follow-up observations with the Extremely Large Telescope (ELT) by taking one data point every 10 days (Vermin et al. 2011). In these simulations, we numerically calculate the Fisher and covariance matrices to evaluate the probability of discerning parallax amplitudes through astrometric and photometric observations. In Section 4, we explain the results and conclude.

## 2. Parallax Effect in Astrometric Microlensing

In this section, we aim to answer this question: in what kind of microlensing events are the parallax amplitudes in astrometric deflections more realizable than those in the magnification curves? With this aim, in Section 2.1, we first review our formalism for generating astrometric microlensing events by considering the parallax effect. Then, in Sections 2.2 and 2.3, we simulate these events and statistically evaluate parallax-induced perturbations.

### 2.1. Formalism

In a gravitational microlensing event, the light of a background star is temporarily magnified due to passing through the gravitational potential of a collinear and foreground massive object (Einstein 1936). In this phenomenon from a background star, two images are formed whose angular positions and magnification factors are, respectively,

$$\theta_{\pm} = \frac{u \pm \sqrt{u^2 + 4}}{2} \theta_E \hat{u}, \quad A_{\pm} = \frac{1}{2} \left( \frac{u^2 + 2}{u\sqrt{u^2 + 4}} \pm 1 \right), \quad (1)$$

where  $u$  is the angular distance of the source star from the lens object normalized to the angular Einstein radius (i.e.,  $\theta_E$ , the angular radius of the images' ring when the lens, source star, and observer are completely aligned), and  $\hat{u}$  is a unit vector representing the direction of  $u$  projected on the sky plane.

Hence, the locations of two images and the source star are over a straight line in the sky plane. The angular distance of these images ( $\simeq 2\theta_E$ ) is too small to be resolved because  $\theta_E$  is on milliarcsecond scales. For instance, for a common lens object (e.g., an M dwarf star) in the Galactic disk ( $D_1 \simeq 4$  kpc, where  $D_1$  is the lens distance from the observer) while the source star is inside the GB (i.e., the source distance from the observer is  $D_s \simeq 8$  kpc), it is given by

$$\theta_E = \sqrt{\kappa \pi_{\text{rel}} M_1} = 0.78(\text{mas}) \sqrt{\frac{M_1}{0.3M_{\odot}}} \sqrt{\frac{\pi_{\text{rel}}}{0.25 \text{ mas}}}, \quad (2)$$

where  $\pi_{\text{rel}} = au(1/D_1 - 1/D_s)$  is the so-called relative parallax,  $au$  is astronomical units, and  $\kappa = 8.14 \text{ mas } M_{\odot}^{-1}$  has a constant value. Therefore, we receive the total light of images which is magnified, the so-called gravitational microlensing event. The magnification factor due to both images is given by

$$A = \frac{u^2 + 2}{u\sqrt{u^2 + 4}}. \quad (3)$$

In a microlensing event, in addition to the light magnification of a background star, the brightness center of these images does not coincide with the source's center. The astrometric deflection in the source position is given by (Hog et al. 1995; Miyamoto & Yoshii 1995; Walker 1995; Miralda-Escude 1996)

$$\delta\theta = \frac{\theta_+ A_+ + \theta_- A_-}{A_+ + A_-} - u \theta_E = \frac{u \theta_E}{u^2 + 2}, \quad (4)$$

which is a function of time. This shift is a dimensional parameter and could be used for measuring the angular Einstein radius.

By ignoring the motion of the observer around the Sun (i.e., we first assume that the observer is the Sun), the vector of the relative lens–source position in the heliocentric frame,  $\mathbf{u}_{\odot}$ , is expressed as a function of time  $t$ ,

$$\mathbf{u}_{\odot} = \begin{pmatrix} (t - t_0)/t_E \\ u_0 \end{pmatrix}, \quad (5)$$

where  $u_0$  is the lens impact parameter (the closest lens–source distance),  $t_0$  is the time of the closest approach, and  $t_E = \theta_E/\mu_{\text{rel},\odot}$  is the so-called Einstein crossing time, the time of crossing the angular Einstein radius. Here  $\mu_{\text{rel},\odot}$  is the angular lens–source relative velocity as measured in the heliocentric frame.

We now add the Earth's motion around the Sun (by assuming that the observer is on the Earth), the so-called parallax effect. In gravitational microlensing events, the parallax effect alters the angular lens–source relative velocity as

$$\boldsymbol{\mu}_{\text{rel}} = \boldsymbol{\mu}_{\text{rel},\odot} + \frac{\pi_{\text{rel}}}{\text{au}} \mathbf{v}_{\text{o},\perp}(t), \quad (6)$$

where  $\mathbf{v}_{\text{o},\perp}$  is the vector of the Earth's velocity with respect to the Sun projected on the sky plane (normal to the line of sight). Therefore, the parallax effect changes the vector of the relative lens–source distance as measured from the Earth as

$$\mathbf{u} = \mathbf{u}_{\odot} + \frac{\pi_{\text{E}}}{\text{au}} \int_{t_0}^t dt \mathbf{v}_{\text{o},\perp}(t) = \mathbf{u}_{\odot} + \pi_{\text{E}} \boldsymbol{\Delta}_{\text{o},\text{n}}, \quad (7)$$

where  $\pi_{\text{E}} = \pi_{\text{rel}}/\theta_{\text{E}}$  is the relative lens–source parallax normalized to the angular Einstein radius, and  $\boldsymbol{\Delta}_{\text{o},\text{n}}$  is an extra displacement in the source position with respect to the lens due to the Earth's motion, normalized to astronomical units.

We note that in real observations, the Earth's motion around the Sun is completely known, but (i)  $\pi_{\text{E}}$  and (ii) the angle between the Earth's velocity projected on the sky plane and the source trajectory are unknown. For that reason, the parallax effect includes two new variables in the lensing formalism, i.e.,  $\pi_{\text{E}}$  and  $\xi$ . Since the relative source–lens trajectory projected on the sky plane has a fixed direction (i.e., the Sun and other stars move on straight lines during lensing timescales), we define  $\xi$  as the angle between  $\mathbf{v}_{\text{o},\perp}$  and  $\boldsymbol{\mu}_{\text{rel},\odot}$  at the time of closest approach  $t_0$ .

The second term in Equation (7) changes periodically and causes a periodic perturbation in the magnification curve and astrometric deflection in the source trajectory. The amplitude of this perturbation in the magnification factor is  $\pi_{\text{E}}$  because the magnification factor  $A$  depends only on  $u$ .

The astrometric deflection in the source trajectory by considering the parallax effect is

$$\delta\boldsymbol{\theta} = \delta\boldsymbol{\theta}_0 + \delta\boldsymbol{\theta}_1 = \frac{\mathbf{u}_{\odot} \theta_{\text{E}}}{u^2 + 2} + \frac{\boldsymbol{\Delta}_{\text{o},\text{n}} \pi_{\text{rel}}}{u^2 + 2}, \quad (8)$$

where  $u^2 = u_{\odot}^2 + \pi_{\text{E}}^2 \Delta_{\text{o},\text{n}}^2 + 2\pi_{\text{E}} \mathbf{u}_{\odot} \cdot \boldsymbol{\Delta}_{\text{o},\text{n}}$ . The first term makes an ellipse on the lens plane (with small perturbations), and the second term makes a periodic perturbation over that ellipse. The amplitude of these periodic perturbations is proportional to  $\pi_{\text{rel}}$ . However, the larger the  $\theta_{\text{E}}$ , the higher the detectability of these perturbations. Because (i) the amplitude of the astrometric deflection is proportional to  $\theta_{\text{E}}$  and (ii) the higher  $\theta_{\text{E}}$  makes a lower  $\pi_{\text{E}}$ , the second term in Equation (8) increases. According to Equation (2), long-duration microlensing events due to ISMBHs close to the observer (in comparison with the source distance) are the most suitable ones to realize the parallax effect in their astrometric deflections instead of magnification curves.

Briefly, the parallax effect changes both the magnification factor and the astrometric deflection in the source position (as given by Equations (3) and (4)) in different ways, as follows.

1. These two observing features have different timescales, as they tend to zero by  $u^{-4}$  and  $u^{-1}$ , respectively (see, e.g., Dominik & Sahu 2000; Sajadian 2014). By getting the source star away from the gravitational potential of the lens object, the astrometric deflection in the source position tends to zero very slowly. The slow evolution of

the astrometric shift is beneficial to realize annual parallax amplitude.

2. The amplitudes of the parallax-induced perturbations in the magnification factor and the astrometric deflection are proportional to  $\pi_{\text{E}}$  and  $\pi_{\text{rel}}$ , respectively. Considering the fact that, for realizing the astrometric deflection itself,  $\theta_{\text{E}}$  should be large, in long-duration microlensing events due to ISMBHs very close to the observer, the parallax amplitude could be discerned in astrometric deflections instead of magnification factors.
3. When  $u = u_0$ , the magnification factor is maximum, whereas for  $u = \sqrt{2}$ , the astrometric deviation is maximum. Hence, discerning the parallax-induced perturbation in the magnification factor and astrometric deflection can be done with a higher probability when  $u \ll 1$  and  $u \simeq 1$ , respectively. This point can be found in Figure 5.

So, searching the parallax effect in the astrometric deflection instead of the magnification factor would be possible in long-duration microlensing events due to massive and close lens objects (e.g., stellar- or intermediate-mass black holes). These points will be verified numerically in the next subsections by performing simulations of microlensing events toward the GB and LMC.

## 2.2. Astrometric Microlensing toward the GB

Using the introduced formalism, we simulate possible astrometric microlensing events toward the GB by considering the annual parallax effect (based on their distribution functions). We justify our simulation according to the Roman observing strategy. We assume that the Roman orbit is a circle of radius 1.01 au centered on the Sun (at the second Sun–Earth Lagrange point, L2). However, in the simulation, we increase the observing time to 19 yr because the astrometric deflection tends to zero very slowly.

To simulate a microlensing event, we first choose the source distance from the observer,  $D_{\text{s}}$ , using the projected mass density in each line of sight,  $dM(D_{\text{s}}, l, b)/dD_{\text{s}} = d\Omega D_{\text{s}}^2 (\rho_{\text{b}} + \rho_{\text{d}} + \rho_{\text{h}})$ . Here  $(l, b)$  are the Galactic longitude and latitude, respectively, and  $\rho_{\text{b}}$ ,  $\rho_{\text{d}}$ , and  $\rho_{\text{h}}$  are the stellar densities of the GB, disks, and halo, respectively. The physical properties of the source stars (absolute magnitude, mass, radius, type, etc.) are determined according to the Galactic Besançon model<sup>2</sup> (Robin et al. 2003, 2012).

The distance of the lens object from the observer depends on  $D_{\text{s}}$  and the given line of sight  $(l, b)$ . We determine the lens distance from the observer using the microlensing event rate, i.e.,  $\Gamma \propto R_{\text{E}} (\rho_{\text{b}} + \rho_{\text{d}} + \rho_{\text{h}}) v_{\text{rel}}$ , where  $R_{\text{E}} = D_{\text{l}} \theta_{\text{E}}$ ,  $v_{\text{rel}} = D_{\text{l}} \mu_{\text{rel}}$ , and  $\mu_{\text{rel}}$  is the size of the angular relative lens–source velocity (given by Equation (6)). In order to simulate long-duration microlensing events due to ISMBHs, we select the lens mass uniformly from the range  $M_{\text{l}} \in [2, 50] M_{\odot}$  (Sicilia et al. 2022).

Three examples of astrometric deflections in the source trajectories are depicted in the top panels of Figure 1. In these panels, solid black and dashed blue curves are astrometric deflections without and with considering the parallax effect. Dotted magenta curves represent the first term in Equation (8). These magenta curves show that parallax-induced perturbations are mostly generated by the second term of Equation (8). At the

<sup>2</sup> <https://model.obs-besancon.fr/>

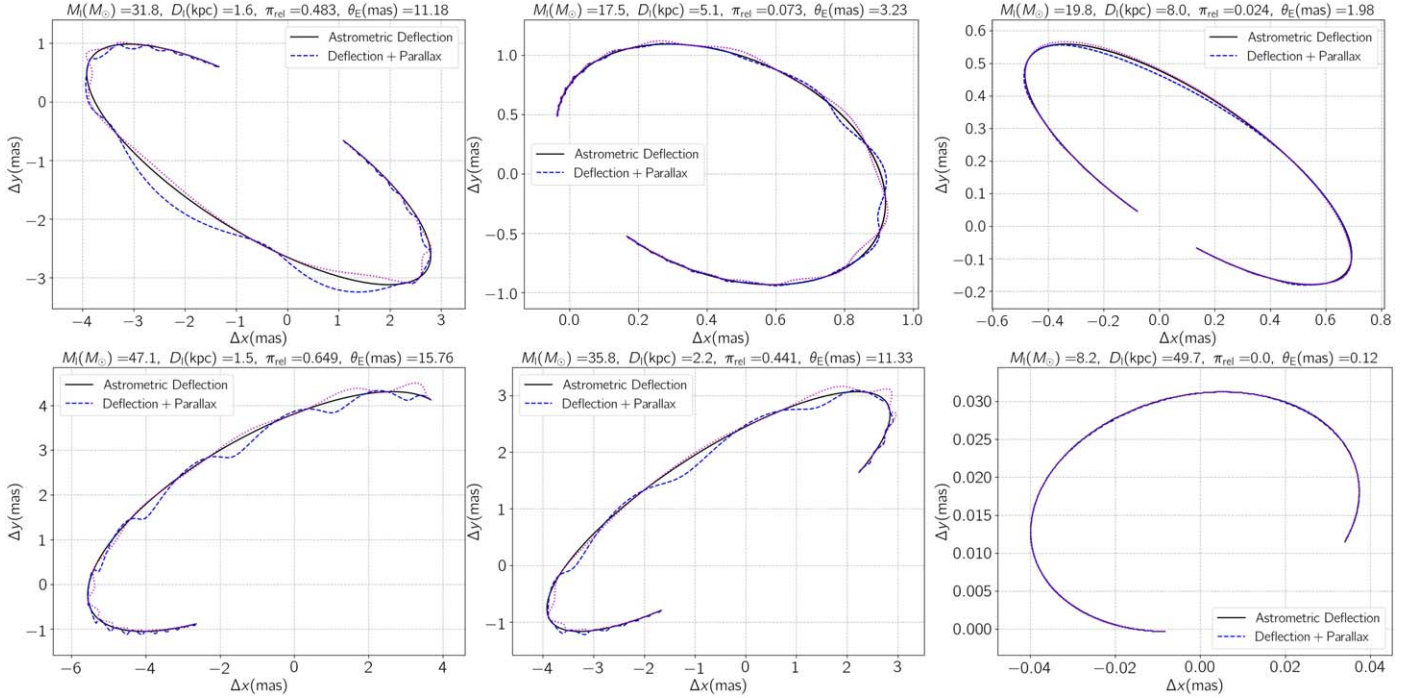


**Figure 1.** Examples of astrometric deflections in source trajectories in long-duration microlensing events toward the GB (top panels) and LMC (bottom panels) due to ISMBHs by ignoring (solid black curves) and including (dashed blue curves) the parallax effect. The dotted magenta curves are the first term in the astrometric deflection given by Equation (8), i.e.,  $\delta\theta_0$ . Their parameters are given at the top of the panels.

top of the panels, the relevant parameters are reported. These panels confirm the results in Section 2.1.

Concerning the detectability of parallax-induced perturbations in astrometric deflections, we evaluate a statistical parameter. For each microlensing event, in the time interval  $[-1.5t_E, 1.5t_E]$ , we numerically calculate the rms of deviations in the astrometric deflections, i.e.,

$$\delta\theta_{\text{rms}} = \sqrt{\langle (\delta\theta(t) - \delta\theta_{\odot}(t))^2 \rangle_t}, \quad (9)$$

where  $\delta\theta_{\odot}(t)$  is the astrometric deflection without the parallax effect. This parameter shows the scale of the parallax-induced deviations in the astrometric deflections. We simulate a large number of astrometric microlensing events due to massive lens objects toward the GB and extract the detectable events in the Roman observations. Then, we determine  $\delta\theta_{\text{rms}}$  for each detectable event.

In the top panels of Figure 2, we represent the scatter plots of  $\delta\theta_{\text{rms}}$  versus  $D_l$ ,  $\log_{10}[\pi_{\text{rel}}(\text{mas})]$ , and  $\log_{10}[\theta_E(\text{mas})]$  (left to right). Accordingly, the parallax-induced perturbations in the astrometric deflections are considerable when the lens is very close to the observer. Although the size of these perturbations does not depend on the lens mass, they are detected in the events due to more massive lenses with a higher probability because the astrometric deflections are scaled with  $\theta_E \propto \sqrt{M_l}$ . The bottom middle and right panels of Figure 2 manifest that  $\delta\theta_{\text{rms}} \propto \pi_{\text{rel}} \propto \theta_E^2$ .

For the microlensing observations toward the MCs, the parallax perturbations in the astrometric deflections should be even higher because the lens object can be in the Galactic halo ( $D_l \sim 2$  kpc) and the source stars are inside the LMC ( $D_s \sim 50$  kpc), which results in a large relative parallax, i.e.,  $\pi_{\text{rel}} \sim 0.48$  mas. We study this point in the next subsection.

### 2.3. Astrometric Microlensing toward the LMC

Microlensing observations toward the LMC were first proposed by Paczynski (1986) to determine the contribution of MACHOs in the Galactic halo. The upcoming LSST telescope will monitor the LMC with a 3 day cadence in six filters, *ugrizy*, during its mission. This telescope will discern a considerable number of long-duration microlensing events because of its long observing time (i.e., 10 yr). However, its long cadence is such that it is simply not going to be able to resolve the hours/days anomalies typical of planetary microlensing events. In this subsection, we simulate astrometric microlensing events toward the LMC by considering the parallax effect.

The LMC celestial coordinates are (R.A., decl.) = (80°9, −68°2), and its distance from the observer is 49.97 kpc. For simulating potential microlensing events toward the LMC, we include stellar spatial distributions due to the LMC’s disk, bulge, and halo, as given by Gyuk et al. (2000) and rewritten in Appendix (A) of Sajadian (2021a). We assume that the photometric properties of the LMC stars are the same as those in our galaxy. The extinction toward the LMC is ignorable, except for its central part (see, e.g., Dobashi et al. 2008). For the central part of LMC, we consider the V-band extinction in the range of  $A_V \in [1.6, 2.1]$  mag uniformly. We simulate microlensing events toward a square of angular side 4° centered on the LMC’s center.

Three examples of simulated astrometric deflections in microlensing events toward the LMC are represented in the bottom panels of Figure 1. The last one is a self-lensing event (its lens object is inside the LMC), and the two others are halo-lensing ones (their lens objects are in the Galactic halo). Accordingly, the parallax effect is realizable in astrometric deflections of halo-lensing events made by massive lens objects.

In the bottom panels of Figure 2, we show the scatter plots of  $\delta\theta_{\text{rms}}$  versus the lens distance,  $\log_{10}[\pi_{\text{rel}}(\text{mas})]$ , and  $\log_{10}[\theta_E(\text{mas})]$ . In these panels, halo-lensing events are

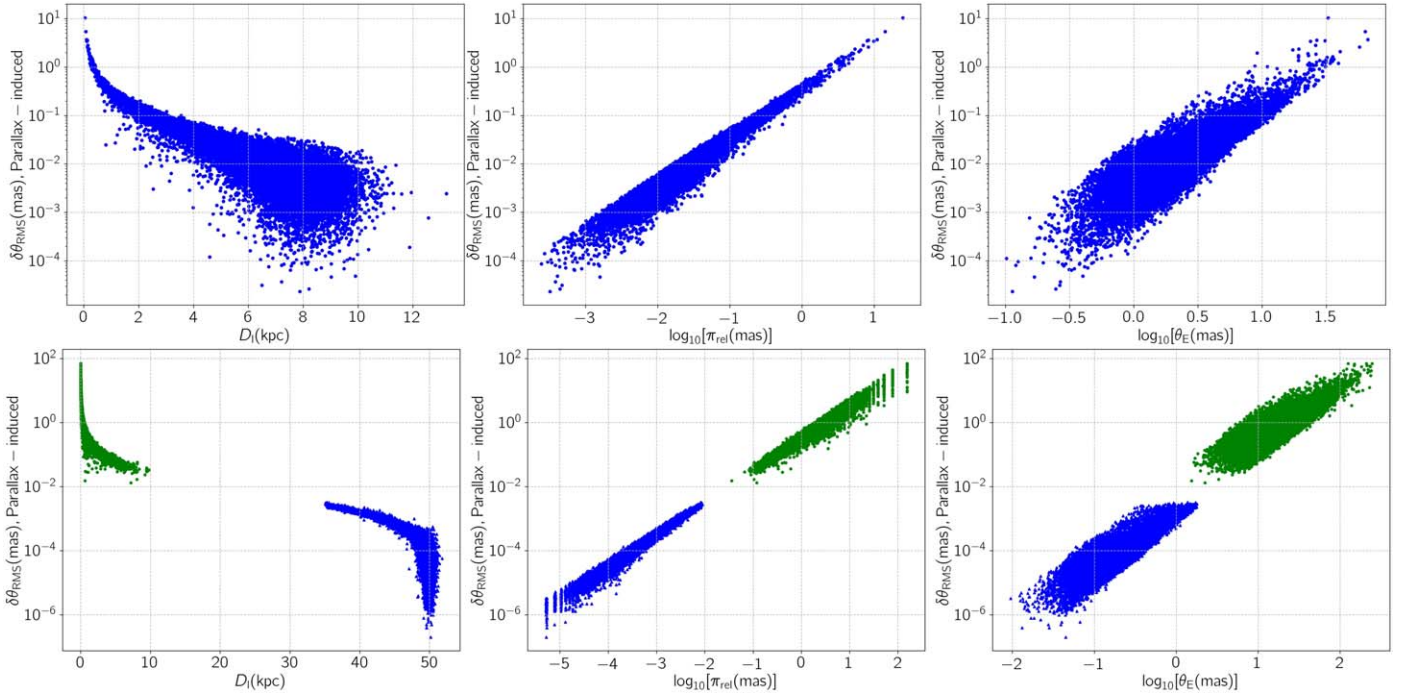


**Figure 2.** Scatter plots of  $\delta\theta_{\text{rms}}$  (given by Equation (9)) for a sample of astrometric microlensing events due to ISMBHs toward the GB (top panels) and LMC (bottom panels) vs.  $D_l$ (kpc),  $\log_{10}[\pi_{\text{rel}}]$ (mas), and  $\log_{10}[\theta_E]$ (mas) (left to right). In the bottom panels, self- and halo-lensing events are specified with blue triangles and green circles, respectively.

specified with green circles, and self-lensing events are denoted with blue triangles. On average, relative parallax amplitude ( $\pi_{\text{rel}}$ ), angular Einstein radius, and as a result  $\delta\theta_{\text{rms}}$  in halo-lensing events are larger than those due to self-lensing events by more than 2 orders of magnitude.

Also, by changing the observational direction from the GB to the LMC,  $\delta\theta_{\text{rms}}$  enhances by more than 1 order of magnitude. The astrometric accuracy of the ELT<sup>3</sup> (Vermin et al. 2011; Tamai & Spyromilio 2014), which is under construction, for a bright star with a  $K$ -band apparent magnitude of 18–19 mag reaches  $50 \mu\text{as}$ . Hence, this telescope, by following up long-duration events toward the LMC, can detect not only astrometric deflections in source trajectories but also their parallax-induced deviations. Measuring  $\theta_E$  and  $\pi_{\text{rel}}$  will specify the lens mass and its distance uniquely. We study this point quantitatively in the next section.

### 3. Simulations of Astrometric Microlensing by Roman and LSST

In the previous section, we found that the parallax effect could make considerable deviations in lensing-induced astrometric deflections due to massive and close lens objects. Here we aim to evaluate the detectability of these parallax-induced deviations and their characterizations.

Extracting parallax amplitudes depends on observing the photometric and astrometric accuracies, cadence, and time interval. Therefore, evaluating the efficiency of discerning and characterizing parallax amplitudes in astrometric deflections or microlensing light curves needs comprehensive simulations of these events by generating synthetic data points based on real observations.

**Table 1**

The Descriptions of Monte Carlo Simulations (A), (B), and (C), Explained in Section 3

Simulation	Observations	Telescope	$T_{\text{obs}}$ (yr)	Cadence	Filter
(A)	Survey	Roman	5	15 minutes	W149
	Follow-up	Roman	5	10 days	W149
(B)	Survey	Roman	5	15 minutes	W149
	Follow-up	ELT	5	10 days	$K$
(C)	Survey	LSST	10	3 days	<i>ugrizy</i>
	Follow-up	ELT	10	10 days	$K$

For more realistic simulations, we apply observing strategies due to upcoming microlensing surveys. We consider three strategies, which are summarized in Table 1 and explained in the following.

- (A) Survey observations with the Roman telescope toward the GB during six 62 day seasons (its total observing time is 5 yr) with a 15 minute cadence. We also consider some extra observations (1 hr observation every 10 days) during the Roman large seasonal gap and when the bulge is visible for this telescope. The same observing strategy was introduced to study detecting ISMBHs by the Roman telescope in Sajadian & Sahu (2023).
- (B) Survey observations with the Roman telescope and follow-up observations with the ELT in the  $K$  band toward the GB. The ELT will start observations for each event when  $A > 1.34$ . We assume that this telescope will take one data point every 10 days during its observing seasons.
- (C) Survey observations with the LSST telescope toward the LMC and follow-up observations with the ELT. The LSST cadence is planned to be 3 days, and its mission will take 10 yr.

<sup>3</sup> <https://elt.eso.org/>

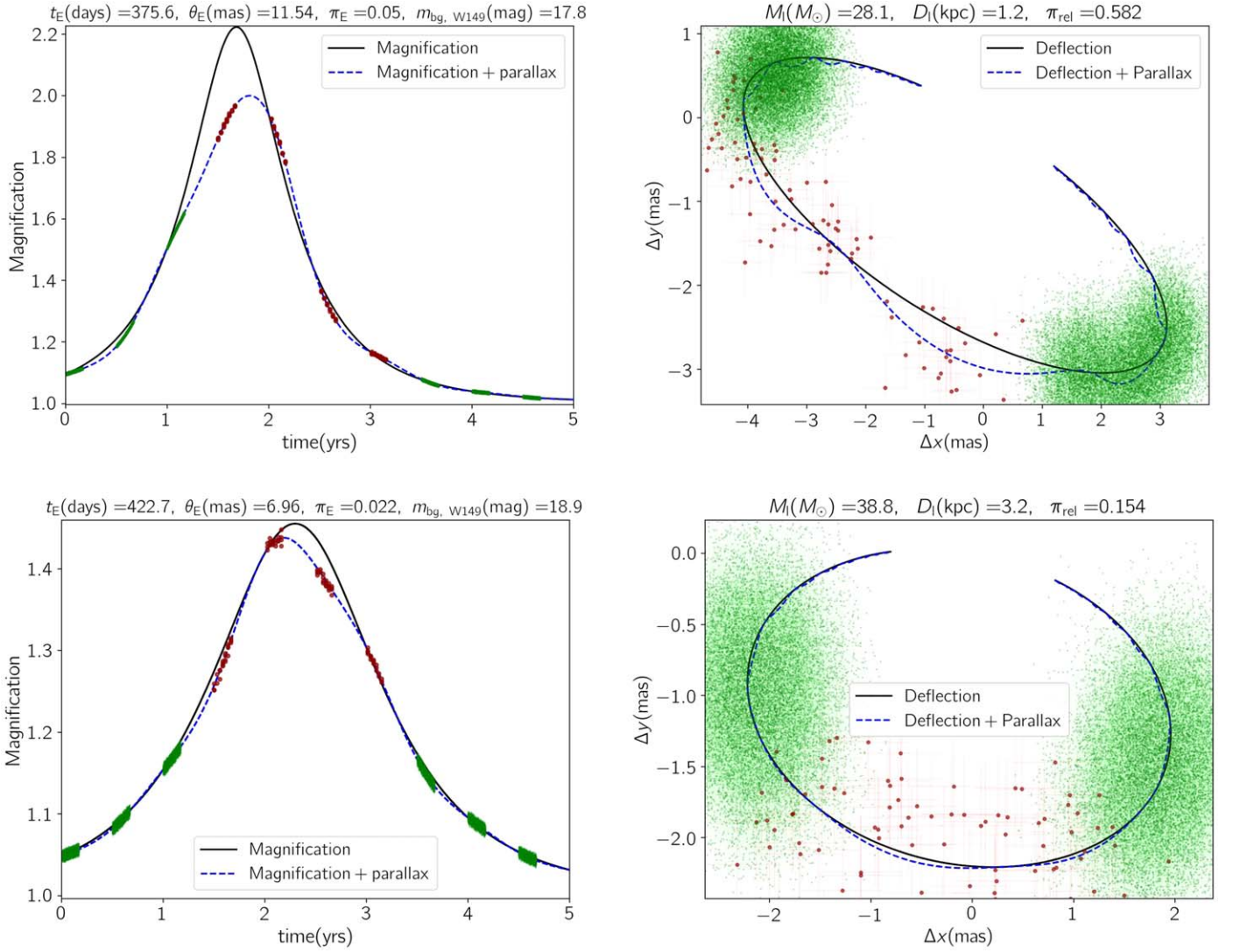


**Figure 3.** Two examples of simulated microlensing events that are detectable with the Roman telescope. For each event, the light curve and astrometric deflection are represented (left and right panels). The green and dark red points are taken by the Roman telescope during its observing seasons and its large seasonal gap, respectively. Their parameters can be found at the top of the panels.

**Table 2**  
The Results of Monte Carlo Simulations (A), (B), and (C), Explained in Table 1

Simulation	$\epsilon_{\theta_E}$ [%]	$\epsilon_{\pi_E}$ [%]	$\epsilon_{\pi_E, \text{Phot}}$ [%]	$\epsilon_{\pi_E, \text{Ast}}$ [%]	$\epsilon_{M_l}$ [%]	$\epsilon_{D_l}$ [%]	$\epsilon_{t_E}$ [%]	$\epsilon$ [%]
Detection threshold = 1%								
(A)	70.65	7.80	7.72	0.36	5.48	21.76	29.73	5.71
(B)	76.71	11.35	11.30	0.78	9.18	29.87	49.78	9.75
(C)	62.14	25.92	8.38	25.08	8.03	18.69	20.88	10.20
Detection threshold = 4%								
(A)	97.47	21.94	21.68	2.16	21.05	46.67	58.40	20.94
(B)	98.25	29.18	29.09	3.76	28.41	59.57	85.78	28.83
(C)	77.12	42.00	22.98	41.09	22.80	47.67	54.64	27.44
Detection threshold = 7%								
(A)	99.36	29.81	29.44	4.05	29.19	57.57	69.29	28.93
(B)	99.61	38.61	38.46	6.55	38.18	71.18	93.34	38.46
(C)	82.78	47.27	29.93	46.10	29.78	59.76	67.97	35.04

**Note.** Here  $\epsilon_a$  refers to the probability of measuring the parameter  $a$  so that its relative error is less than the given threshold. The indices “Phot” and “Ast” in the probability of measuring parallax amplitudes refer to inferring parallax from photometric and astrometric data with a given detection threshold, respectively.

We tune our simulations based on these observing strategies. In the following, we explain the details of these Monte Carlo simulations and the results.

(A) Survey microlensing with Roman. We first tune our simulations for potential survey observations toward the GB with the Roman telescope. We did similar simulations in Sajadian & Sahu (2023). In that paper, we showed that a small number of additional observations, i.e., 1 hr of observations every 10 days when the GB is observable during the large seasonal gap, will improve Roman’s efficiency in detecting and characterizing ISMBHs. In simulation (A), we assume that these extra and sparse data points are taken with Roman.

In the simulation, we take the time of the closest approach  $t_0$  uniformly in the range  $[0, 5]$  yr. The lens impact parameter is also chosen smoothly from the range  $[0, 1]$ . The finite-source effect for microlensing events due to massive lens objects is ignorable because the normalized source radius projected on the lens plane is  $\rho_* \propto 1/\sqrt{M_l}$  and very small. We consider the parallax effect while the calculating light curves and astrometric deflection to compare the errors while extracting the parallax amplitude from each of them. Since the Roman telescope will orbit the Sun from the second Sun–Earth Lagrange point (L2), the radius of its orbit is 1.01 au.

In Monte Carlo simulations from microlensing events detectable by Roman, we remove events with a timescale of  $t_E > 2000$  days because in most of these events, the magnification factors do not reach the baseline during the Roman 5 yr mission.

For calculating the blending effect in all Monte Carlo simulations, we first calculate the average number of background stars inside a stellar point-spread function (PSF) as

$$\bar{N}_* = \Omega_{\text{PSF}} f_b \int_0^{D_s} \left( \frac{\rho_b(x)}{M_b} + \frac{\rho_d(x)}{M_d} + \frac{\rho_h(x)}{M_h} \right) x^2 dx,$$

where  $f_b = 2/3$  is the binary fraction;  $\bar{M}_b$ ,  $\bar{M}_d$ , and  $\bar{M}_h$  are the average masses of stars in the GB, disk, and halo, respectively; and  $\Omega_{\text{PSF}} = \pi(\text{FWHM}/2)^2$  is the area of a typical stellar PSF in the Roman observations. We determine the number of stars using  $N_* = \bar{N}_* + \sigma_{N_*}$ , where  $\sigma_{N_*}$  is chosen using a normal distribution  $\mathcal{N}(0, \sqrt{\bar{N}_*})$ . A common value for FWHM is  $3 \times \text{pixel size}$ , i.e.,  $0''.33$  for the Roman observation.

The Roman photometry accuracy  $\sigma_m$  is a function of stellar apparent magnitude in the W149 filter and was given in Figure 4 of Penny et al. (2019). Stellar absolute magnitudes in W149 are estimated by  $M_{W149} \simeq (M_H + M_J + M_K)/3$ , where  $M_H$ ,  $M_J$ , and  $M_K$  represent the stellar absolute magnitudes in the standard filters  $H$ ,  $J$ , and  $K$ , respectively (see, e.g., Sajadian 2021b). We note that the Galactic Beçançon model gives the stellar absolute magnitudes in the standard filters  $BVRIK$ . We specify the absolute magnitudes in the  $H$  and  $J$  bands using the Dartmouth isochrones<sup>4</sup> (Dotter et al. 2008; Feiden et al. 2011).

We use the 3D extinction map offered by Marshall et al. (2006) and use the following transformation relations to specify extinctions in other bands:  $A_V = 8.47A_K = 8.21A_{K_s} = 1.67A_J = 5.43A_H = 4.44A_{W149}$  (Cardelli et al. 1989). We determine the astrometric accuracy of Roman according to stellar apparent magnitude and using *Jitter* simulations done by S. C.

Novati. We assume that the probability of regular observations with Roman is 90% during its observing seasons.

In Figure 3, two simulated astrometric microlensing events detectable by Roman are represented. The sparse data points during its large seasonal gap are shown in dark red, and the Roman data during its observing seasons are depicted in green. In this figure, the sparse data points help to discern astrometric deflections and, as a result, the Einstein angular radius. The parallax amplitude can be extracted from the Roman photometric data.

After making a big ensemble of these events, we extract the detectable events in the Roman observations. We have two criteria for detectability: (i)  $\Delta\chi^2 = |\chi_{\text{real}}^2 - \chi_{\text{base}}^2| > 800$ , where  $\chi_{\text{real}}^2$  and  $\chi_{\text{base}}^2$  are  $\chi^2$  values from fitting the real model and the baseline, respectively; and (ii) three data points should be above the baseline by at least  $4\sigma$ , where  $\sigma$  is the photometric accuracy.

We numerically calculate the photometric and astrometric Fisher matrices separately, i.e.,  $\mathcal{A}$  and  $\mathcal{B}$  for each detectable event. In this regard, the observable parameters that affect the magnification curves and astrometric deflections are  $t_0$ ,  $u_0$ ,  $t_E$ ,  $\xi$ ,  $f_b$ ,  $m_{\text{base}}$ , and  $\theta_E$ ,  $\pi_E$ , and  $\mu_s$ , respectively. We embed  $\pi_E$  into both lists to compare the photometric and astrometric errors while extracting the parallax amplitude.

In fact, real astronomical data points determine the projected source trajectory on the sky plane, which is

$$\theta_s(t) = u_0 \theta_E + \mu_s(t - t_0) - \pi_s \Delta_{\text{o,n}}(t) + \delta\theta(t), \quad (10)$$

where  $\mu_s$  is the angular velocity of the source star, and  $\pi_s = 1.01 \text{ au}/D_s$  is the so-called source parallax amplitude when the observer is Roman. The source parallax amplitude ( $\pi_s$ ) is very small and ignorable. Hence, the parallax-induced perturbations mostly alter the last term (i.e., the astrometric deflection). Throughout the paper and in Figures 1, 3, 6, and 7, we only show the last term (the astrometric deflection) so that the parallax-induced deviations get highlighted. However, while calculating the astrometric Fisher matrix ( $\mathcal{B}$ ), we numerically calculate the derivatives of the source trajectory  $\theta_s(t)$  with respect to its parameters.

The results from this simulation are reported in Table 2. In this table,  $\epsilon_a$  is the probability (or efficiency) of measuring the parameter  $a$  with a relative error of less than the given thresholds (i.e., 1%, 4%, and 7%). The indices “Phot” and “Ast” for  $\epsilon_{\pi_E}$  refer to measuring parallax amplitudes from photometric and astrometric data, respectively. The last column is the probability of simultaneously measuring three parameters,  $\theta_E$ ,  $\pi_E$ , and  $t_E$ , with relative errors of less than the given threshold. These parameters uniquely offer the lens mass, lens distance, and lens–source relative velocity. The relations to calculate the errors can be found in Sajadian & Sahu (2023), and we do not repeat them here.

The normalized distributions (NDs) of relative errors in the parallax amplitude,  $\sigma_{\pi_E}/\pi_E$ , extracted from covariance matrices  $\mathcal{A}^{-1}$  (based on photometric data) and  $\mathcal{B}^{-1}$  (based on astrometric data) are depicted in Figure 4 in green and purple, respectively.

Accordingly, in long-duration microlensing events toward the GB detectable by the Roman telescope, the parallax can be extracted from light curves much more than from astrometric deflections (10 times). This point can be seen in Figure 3.

<sup>4</sup> <http://stellar.dartmouth.edu/>

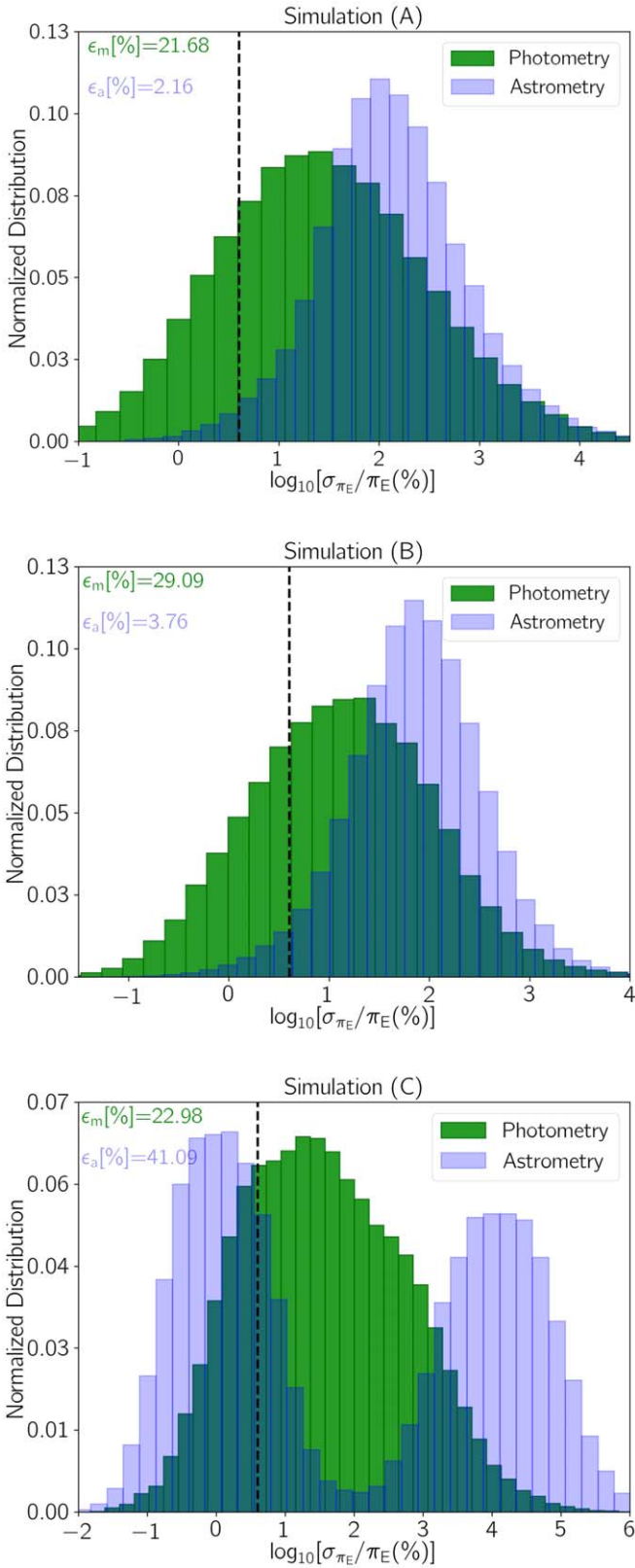


**Figure 4.** The NDs of relative errors in the parallax amplitudes, as measured through photometric (green) and astrometric (purple) observations based on simulations (A), (B), and (C), from top to bottom. The dashed black lines determine the threshold amount  $\sigma_{\pi_E}/\pi_E = 4\%$ . The fractions of events with relative parallax errors of less than 4% are given inside the panels.

To determine in what kind of simulated events parallax amplitudes could be measured through astrometric observations, in the top panels of Figure 5, we show the NDs of  $\log_{10}[\theta_E(\text{mas})]$ ,  $u_0$ , and  $\log_{10}[\pi_{\text{rel}}(\text{mas})]$  due to events that are detectable by Roman with green filled distributions. In these figures, red lines represent the NDs of these parameters due to the events in which  $\pi_E$  can be measured (with relative errors of less than 4%) through either photometric or astrometric data. Blue and black lines are NDs due to events with measurable parallax amplitudes through photometric and astrometric data, respectively. Inside each panel, the average values of the parameters from their distributions are given.

Accordingly, in the events with  $\pi_E \gtrsim 0.25$  mas (or a lens distance  $D_1 \lesssim 2.7$  kpc from the observer), measuring parallax amplitudes through astrometric observations is possible. The events with larger  $u_0$  are more favorable to infer parallax amplitudes from astrometric data, whereas in high-magnification events, parallax amplitudes can be measured from light curves. In fact, the magnification factor tends to zero fast as  $u^{-4}$ , whereas the astrometric deflection maximizes when  $u = \sqrt{2}$ .

(B) GB survey observations by Roman with ELT follow-up. The astrometric precision of the ELT is planned to be better than  $50 \mu\text{as}$ . In this simulation, we consider potential follow-up astrometric observations with the ELT from long-duration microlensing events that will be discovered by Roman.

We assume that this telescope will take one data point every 10 days, which is suitable for long-duration microlensing events. For each microlensing event, the ELT observation is started when its magnification factor reaches 1.34.

For the ELT astrometric observations, we assume that it observes microlensing events in the  $K$  band. In terms of the ELT astrometric precision, the statistical astrometric accuracy of a telescope with an aperture  $D$  and in the observing wavelength  $\lambda$  is given by (see, e.g., Tripp et al. 2010)

$$\sigma_{a,1} = \frac{\lambda}{\pi D} \frac{1}{S/N} = 34 \mu\text{as} \frac{\lambda}{2.2 \mu\text{m}} \frac{42\text{m}}{D} \frac{100}{S/N}, \quad (11)$$

where  $S/N$  is the signal-to-noise ratio. Hence, for the ELT observations with  $S/N = 100$  in the  $K$  band by the Multi-adaptive optics Imaging CAmera for Deep Observations (MICADO,<sup>5</sup> Davies et al. 2021), the statistical astrometric precision will be  $\simeq 34 \mu\text{as}$ . We add the systematic error ( $\sim 10 \mu\text{as}$ ) to this statistical accuracy. Therefore, for a source star with an apparent magnitude of  $m_K \simeq 18\text{--}19$  mag, the MICADO astrometric accuracy reaches  $\sim 50 \mu\text{as}$ . Fiorentino et al. (2020) modeled the images that would be taken by MICADO/ELT from globular clusters and found a more practical relation between the apparent magnitude of stars in the  $K$ -band filter and the MICADO astrometric precision adjusted for a 20 minute exposure time, which was given in their second table. Throughout the paper, we use their results to estimate the ELT astrometric accuracy in the  $K$ -band filter.

We consider a 5 month seasonal gap annually for the ELT. Also, this telescope can take data from stars with a  $K$ -band apparent magnitude in the range  $m_K \in [12, 23]$  mag (its

<sup>5</sup> <https://elt.eso.org/instrument/MICADO/>



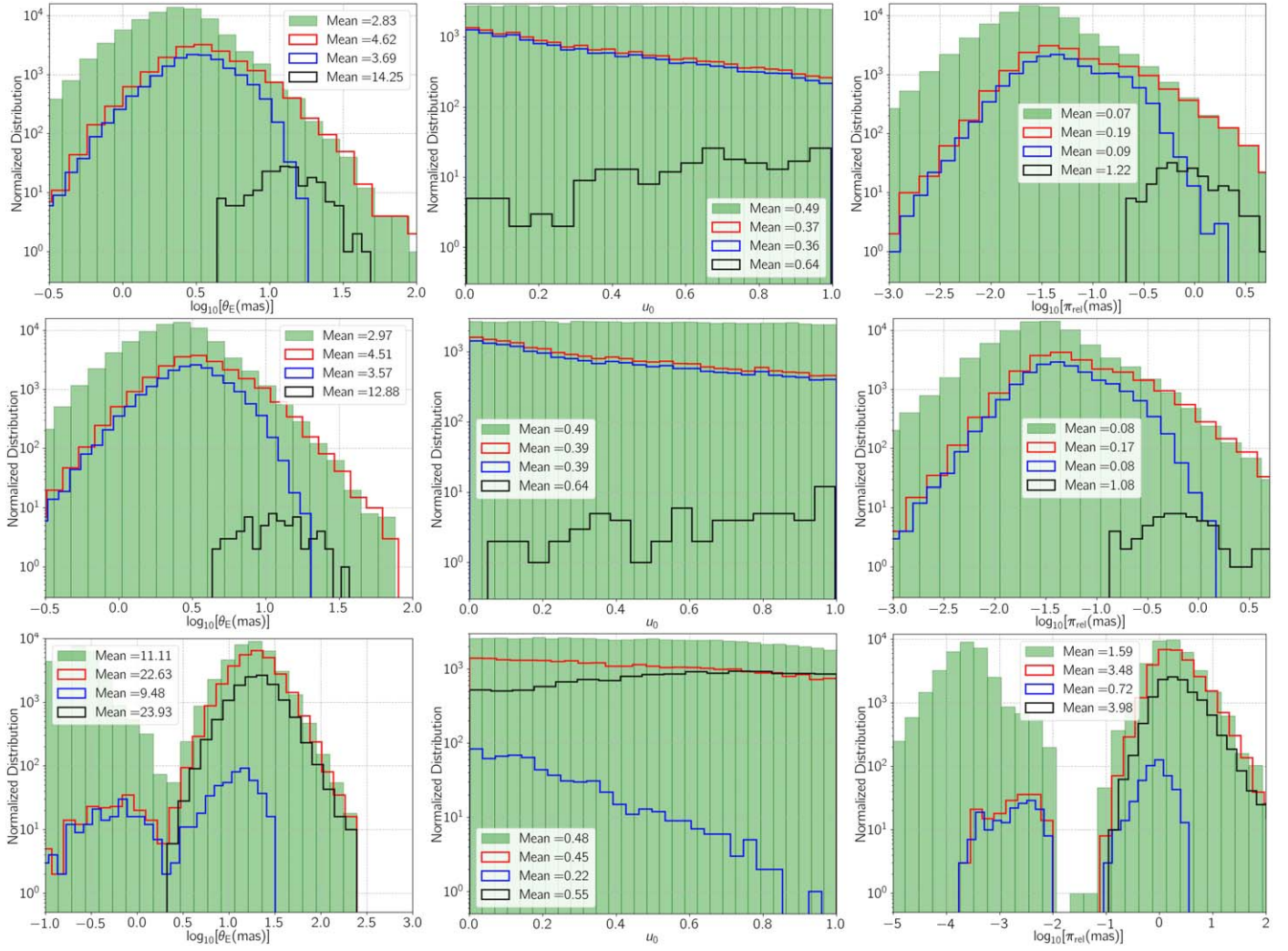


**Figure 5.** The NDs of  $\log_{10}[\theta_E (\text{mas})]$ ,  $u_0$ , and  $\log_{10}[\pi_{\text{rel}} (\text{mas})]$  from simulations (A), (B), and (C) are represented in green from top to bottom. Red lines represent the NDs of these parameters due to events in which  $\pi_E$  can be measured (with a relative error of less than 4%) through either photometric or astrometric data. Blue and black lines are NDs due to events with measurable parallax amplitudes through photometric and astrometric data, respectively. Inside each panel, the average values of the parameters ( $\theta_E$ ,  $u_0$ ,  $\pi_{\text{rel}}$ ) from their distributions are indicated.

saturation and detection thresholds). We assume both probabilities for suitable weather, and regular survey observations are done in 90% of the nights; in 10% of nights some special events will be observed.

In this simulation, extracting lensing parameters and simulating the Roman data is similar to the explanation in simulation (A).

In Figure 6, we show two examples of simulated astrometric microlensing events detected with Roman and ELT. Here dark red points are taken with the ELT. Comparing Figures 3 and 6, one can see the large difference between the astrometric accuracies of Roman and the ELT. Although the ELT data are sparse, they manifest astrometric deflections well. In the first event, discerning the parallax effect in the astrometric deflection is doable because of the ELT astrometric data.

We mention the results from performing Monte Carlo simulation (B) in Table 2. Accordingly, the ELT observations will improve the efficiency in measuring both  $\theta_E$  and  $\pi_E$ . Although the efficiency of discerning parallax amplitudes from astrometric deflections is low for observations toward the GB, some sparse data points with the ELT double this efficiency.

This improvement can be seen by comparing the first two panels of Figure 4.

In the middle row of Figure 5, the NDs of  $\log_{10}[\theta_E (\text{mas})]$ ,  $u_0$ , and  $\log_{10}[\pi_{\text{rel}} (\text{mas})]$  resulting from simulation (B) are depicted. They are similar to the top row (owing to simulation (A)) with small changes.

(C) Survey and follow-up observations with LSST and ELT. The upcoming LSST telescope, which is under construction at the Vera C. Rubin Observatory, Chile, is planned to survey the whole sky with a 3 day cadence (Ivezic et al. 2009). This telescope will observe the LMC during its 10 yr mission and potentially detect several long-duration microlensing events in this direction.

For the LSST observations toward the LMC, we assume follow-up astrometric observations with the ELT with a 10 day cadence. The details of this follow-up astrometric observation are the same as explained in simulation (B).

The LSST data will be taken in six filters, *ugrizy*, which are similar to the filters used by the Sloan Digital Sky Survey (Fukugita et al. 1996; Ivezic et al. 2009). We determine the photometric errors in these filters using the relations explained

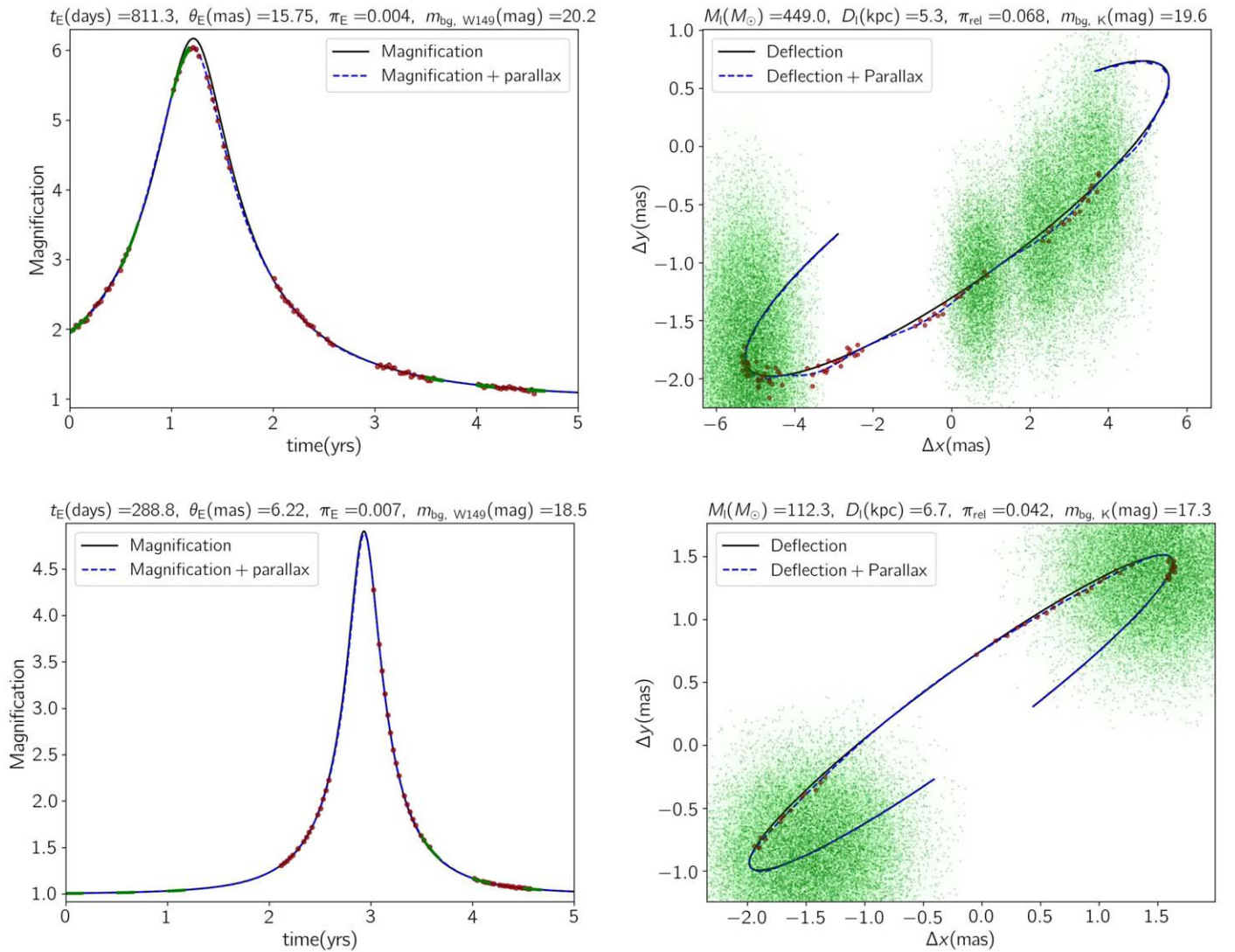


**Figure 6.** Same as Figure 3, but dark red points are hypothetically taken by the ELT in the  $K$  band with a 10 day observing cadence.

in Section 3 of Ivezić et al. (2009). The astrometric accuracy of LSST is also a function of stellar apparent magnitude (see, e.g., Eyer et al. 2012). We assume that both probabilities of suitable weather for observations and doing regular observations with LSST are 90%. The LSST seasonal gap lasts 5 months.

Since the LSST observing time is 10 yr, we ignore microlensing events with  $t_E > 4000$  days. In these events, the magnification factors do not reach the baseline during the LSST observing time. Also, the time of the closest approach is uniformly chosen from the range  $t_0 \in [0, 10]$  yr. Other lensing parameters are determined in the same way as explained in simulation (A). We note that for the LSST observations, the blending parameter is considerable because of the LSST’s observing depth (see, e.g., Sajadian & Poleski 2019).

In Figure 7, we depict two examples of simulated astrometric microlensing events detected with the LSST and ELT. The data points taken by LSST in the  $ugrizy$  filters are shown in purple, blue, dark green, yellowish green, orange, and red, respectively. The data taken by the ELT are shown in dark red.

The first event is halo lensing, and the second is a self-lensing event. In the first event, the parallax effect makes

considerable deviations in both magnification factor and astrometric deflection. Since the ELT data are taken in the domain of the light curve (because of the ELT saturation limit), they only cover the parallax-induced deviations in the astrometric deflection. In this event, the parallax amplitude can only be extracted from its astrometric deflection. In the second event (a self-lensing one), the ELT data manifest the astrometric deflection itself and, as a result,  $\theta_E$ . In this event, the parallax amplitude is not measurable.

We perform this Monte Carlo simulation, denoted simulation (C), and make a large sample of these astrometric microlensing events that are discernible in the LSST observations. The detectability criteria are the same as those mentioned for simulation (A). For each simulated event, we numerically calculate Fisher and covariance matrices. The results can be found in Table 2.

Comparing the results reported in Table 2 toward the LMC, the efficiency of measuring  $\theta_E$  even by considering the ELT follow-up observations is less than that toward the GB by  $\sim 10\%$ . There are three reasons. (i) For self-lensing events,  $\theta_E$  is too small (see Figure 2). (ii) The LSST telescope can discern

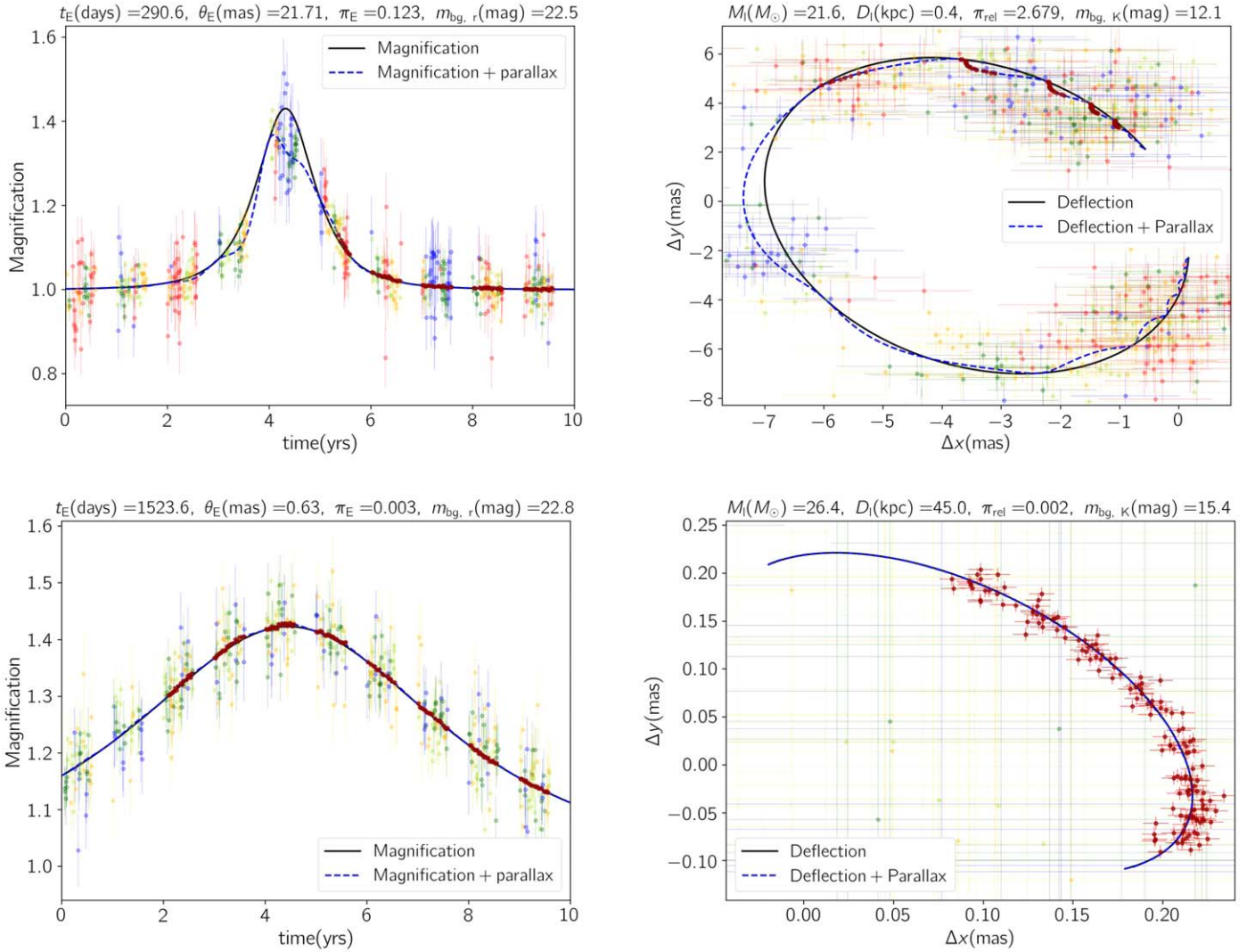


**Figure 7.** Same as Figure 3 but for observations toward the LMC with LSST. The simulated data points taken by LSST in the *ugrizy* filters are shown with purple, blue, dark green, yellowish green, orange, and red, respectively. The data taken with the ELT are depicted in dark red. The observing cadences for the LSST and ELT data are 3 and 10 days, respectively.

faint source stars with an *r*-band apparent magnitude  $m_r \in [16, 24.3]$  mag, so most of the source stars in detectable microlensing events (by the LSST observations) are faint. That means that the efficiencies for measuring parameters from photometric and astrometric data (e.g.,  $u_0$ ,  $t_E$ ,  $\pi_E$ , and  $\theta_E$ ) are lower than those for measuring parameters from the Roman data. (iii) The maximum number of LSST data points during its mission with a 3 day cadence is 708, whereas the maximum number of Roman data points for a microlensing event during six 62 day seasons is 35,700. While calculating Fisher and covariance matrices, higher numbers of data points offer lower errors.

Nevertheless, the efficiency of measuring  $\pi_E$  in microlensing events toward the LMC is more than the efficiency in events toward the GB by  $\sim 13\%$ . Toward the LMC, extracting parallax amplitudes from astrometric deflections is more efficient than taking them from light curves. According to the last panels of Figure 5, there are two kinds of events toward the LMC with very different  $\pi_{\text{rel}}$  values: self- and halo-lensing ones. The second class has large  $\pi_{\text{rel}}$  values and is suitable to determine parallax amplitudes from astrometric data.

Hence, through observations toward the LMC by LSST, efficiencies for extracting  $\theta_E$  and  $t_E$  are lower, and those for extracting  $\pi_E$  are higher in comparison with observations toward the GB with Roman. For that reason, the efficiencies of measuring these three parameters simultaneously through both observations are the same.

The bottom panels of Figure 5 manifest that by decreasing the lens impact parameter, and the efficiency of specifying parallax amplitudes from light curves improves by 2 orders of magnitude.

#### 4. Conclusions

In microlensing events due to massive lens objects (e.g., ISMBHs), measuring parallax amplitudes from their magnification curves is a challenge because the parallax amplitude in these light curves decreases by the lens mass as  $\pi_E \propto 1/\sqrt{M_l}$ . Although these massive lenses make long-duration events in comparison to the Earth's orbital period, they have small parallax amplitudes.

In this work, we studied the possibility of measuring parallax amplitudes from astrometric deflections instead of light curves.

We found that parallax-induced deviations in astrometric deflections are proportional to  $\pi_{\text{rel}}$  but not  $\pi_{\text{E}}$ . However, for detecting these second-order effects, the astrometric deflections themselves should be measurable. Hence, events with large  $\theta_{\text{E}}$  and  $\pi_{\text{rel}}$  are suitable for measuring parallax amplitudes from astrometric data. The best events are long-duration microlensing events toward the LMC due to ISMBHs inside the Galactic halo. In these events, on average, parallax-induced deviations reach  $\sim 10\text{--}100$  mas (see Figure 2). The largest parallax-induced deviations on astrometric deflections occur when  $u \simeq \sqrt{2}$  (at the light-curve domain).

To quantitatively study the detectability of parallax amplitudes in astrometric measurements, we have done three realistic Monte Carlo simulations based on upcoming microlensing surveys, as follows. Simulation (A) includes Galactic bulge (GB) survey microlensing observations with Roman during its 5 yr mission. In this simulation, we assume that the Roman telescope itself would take some sparse data points (1 hr of observation every 10 days) during its large seasonal gap and when the GB is observable. Simulation (B) includes GB survey microlensing observations with the Roman telescope and follow-up observations with the ELT in the  $K$  band. We assume that the ELT would take one data point every 10 days. Simulation (C) includes LSST observations toward the LMC during its 10 yr mission and follow-up observations with the ELT by taking one data point every 10 days.

In the simulations, for each event, we numerically calculated Fisher and covariance matrices based on synthetic photometric and astrometric data points and then estimated the errors. We included the parallax effect in both the magnification factors and astrometric deflections in source trajectories. The results of these simulations are reported in Table 2.

Accordingly, for observations toward the GB and in events due to ISMBHs at a distance  $D_1 \lesssim 2.7$  kpc from the observer, measuring parallax amplitudes through astrometric deflections is possible. However, for microlensing events toward the GB, the efficiency of measuring parallax amplitudes (with relative errors of less than 4%) from astrometric deflections is only 2%. This efficiency is doubled by adding the ELT sparse data points.

In the LSST observations toward the LMC, the efficiency of measuring the parallax amplitudes increases by more than 13%. Toward the LMC, and especially in halo-lensing events, extracting parallax amplitudes from astrometric deflections is more efficient (by 18%) than extracting them from light curves.

Briefly, through observations toward the LMC by LSST, the efficiencies for extracting  $\theta_{\text{E}}$  and  $t_{\text{E}}$  are lower (because LSST will mostly detect microlensing events of faint source stars, and its cadence is long), and for extracting parallax amplitudes, the efficiency is higher in comparison to observations toward the GB with Roman. Hence, the efficiencies of measuring three parameters simultaneously through both observations are in the same range.

### Acknowledgments

The source codes that have been developed for this work can be found in GitHub, [https://github.com/SSajadian54/Parallax\\_Astrometry](https://github.com/SSajadian54/Parallax_Astrometry), and a copy has been deposited to Zenodo (Sajadian et al. 2023).

### ORCID iDs

Sedighe Sajadian  <https://orcid.org/0000-0002-0167-3595>

### References

- Agol, E., Kamionkowski, M., Koopmans, L. V. E., & Blandford, R. D. 2002, *ApJL*, **576**, L131
- Albrow, M., Birch, P., Caldwell, J., et al. 1996, in IAU Symp. 173, *Astrophysical Applications of Gravitational Lensing*, ed. C. S. Kochanek & J. N. Hewitt (Dordrecht: Kluwer), 227
- Alcock, C., Allsman, R. A., Alves, D., et al. 1998, *ApJL*, **499**, L9
- Alcock, C., Allsman, R. A., Alves, D. R., et al. 2000a, *ApJ*, **542**, 281
- Alcock, C., Allsman, R. A., Alves, D. R., et al. 2000b, *ApJ*, **541**, 734
- Aubourg, E., Bairey, P., Brehin, S., et al. 1993, *Msngr*, **72**, 20
- Bennett, D. P., Becker, A. C., Quinn, J. L., et al. 2002, *ApJ*, **579**, 639
- Bhattacharya, A., Beaulieu, J. P., Bennett, D. P., et al. 2018, *AJ*, **156**, 289
- Cardelli, J. A., Clayton, G. C., & Mathis, J. S. 1989, *ApJ*, **345**, 245
- Davies, R., Hörmann, V., Rabien, S., et al. 2021, *Msngr*, **182**, 17
- Dobashi, K., Bernard, J. P., Hughes, A., et al. 2008, *A&A*, **484**, 205
- Dominik, M., & Sahu, K. C. 2000, *ApJ*, **534**, 213
- Dong, S., Mérand, A., Delplancke-Ströbele, F., et al. 2019, *ApJ*, **871**, 70
- Dotter, A., Chaboyer, B., Jevremović, D., et al. 2008, *ApJS*, **178**, 89
- Einstein, A. 1936, *Sci*, **84**, 506
- EROS Collaboration, Derue, F., Afonso, C., et al. 1999, *A&A*, **351**, 87
- Eyer, L., Dubath, P., Mowlavi, N., et al. 2012, in Proc. IAU 282, *From Interacting Binaries to Exoplanets: Essential Modeling Tools*, ed. M. T. Richards & I. Hubeny (Cambridge Univ. Press), 33
- Feiden, G. A., Chaboyer, B., Dotter, A., et al. 2011, *ApJL*, **740**, L25
- Fiorentino, G., Bellazzini, M., Spera, M., et al. 2020, *MNRAS*, **494**, 4413
- Fukugita, M., Ichikawa, T., Gunn, J. E., et al. 1996, *AJ*, **111**, 1748
- Gaudi, B. S. 2012, *ARA&A*, **50**, 411
- Gould, A. 1994, *ApJL*, **421**, L71
- Gould, A., & Loeb, A. 1992, *ApJ*, **396**, 104
- Gyuk, G., Dalal, N., & Griest, K. 2000, *ApJ*, **535**, 90
- Hog, E., Novikov, I. D., & Polnarev, A. G. 1995, *A&A*, **294**, 287
- Ivezic, Z., Tyson, J. A., Axelrod, T., et al. 2009, *BAAS*, **41**, AAS Meeting Abstracts, 213, 366
- Karolinski, N., & Zhu, W. 2020, *MNRAS*, **498**, L25
- Kiraga, M., & Paczynski, B. 1994, *ApJL*, **430**, L101
- Lam, C. Y., Lu, J. R., Udalski, A., et al. 2022, *ApJL*, **933**, L23
- Lasserre, T., Afonso, C., Albert, J. N., et al. 2000, *A&A*, **355**, L39
- Lu, J. R., Sinukoff, E., Ofek, E. O., Udalski, A., & Kozłowski, S. 2016, *ApJ*, **830**, 41
- Mao, S., & Paczynski, B. 1991, *ApJL*, **374**, L37
- Mao, S., Smith, M. C., Woźniak, P., et al. 2002, *MNRAS*, **329**, 349
- Marshall, D. J., Robin, A. C., Reylé, C., Schultheis, M., & Picaud, S. 2006, *A&A*, **453**, 635
- Miralda-Escude, J. 1996, *ApJL*, **470**, L113
- Miyamoto, M., & Yoshii, Y. 1995, *AJ*, **110**, 1427
- Moniez, M., Sajadian, S., Karami, M., Rahvar, S., & Ansari, R. 2017, *A&A*, **604**, A124
- Mróz, P., Udalski, A., Skowron, J., et al. 2017, *Natur*, **548**, 183
- Paczynski, B. 1986, *ApJ*, **304**, 1
- Penny, M. T., Gaudi, B. S., Kerins, E., et al. 2019, *ApJS*, **241**, 3
- Robin, A. C., Marshall, D. J., Schultheis, M., & Reylé, C. 2012, *A&A*, **538**, A106
- Robin, A. C., Reylé, C., Derrière, S., & Picaud, S. 2003, *A&A*, **409**, 523
- Sahu, K. C., Anderson, J., Casertano, S., et al. 2022, *ApJ*, **933**, 83
- Sajadian, S. 2014, *MNRAS*, **439**, 3007
- Sajadian, S. 2021a, *MNRAS*, **506**, 3615
- Sajadian, S. 2021b, *MNRAS*, **508**, 5991
- Sajadian, S. 2023, *MNRAS*, **521**, 6383
- Sajadian, S., Mahmoudzadeh, A., & Moein, S. 2023, *Astrometry\_Parallax*, Version 1, Zenodo, doi:10.5281/zenodo.8342045
- Sajadian, S., & Poleski, R. 2019, *ApJ*, **871**, 205
- Sajadian, S., & Sahu, K. C. 2023, *AJ*, **165**, 96
- Sicilia, A., Lapi, A., Boco, L., et al. 2022, *ApJ*, **924**, 56
- Spergel, D., Gehrels, N., Baltay, C., et al. 2015, arXiv:1503.03757
- Sumi, T., Koshimoto, N., Bennett, D. P., et al. 2023, *AJ*, **166**, 108
- Szymanski, M., Udalski, A., Kaluzny, J., et al. 1994, *AcA*, **44**, 387
- Tamai, R., & Spyromilio, J. 2014, *Proc. SPIE*, **9145**, 91451E
- Terry, S. K., Bennett, D. P., Bhattacharya, A., et al. 2022, *AJ*, **164**, 217
- Trippe, S., Davies, R., Eisenhauer, F., et al. 2010, *MNRAS*, **402**, 1126
- Udalski, A., Zebun, K., Szymanski, M., et al. 2000, *AcA*, **50**, 1
- Vernin, J., Munoz-Tunon, C., Sarazin, M., et al. 2011, *PASP*, **123**, 1334
- Walker, M. A. 1995, *ApJ*, **453**, 37
- Witt, H. J., & Mao, S. 1994, *ApJ*, **430**, 505
- Wu, X.-P. 1994, *ApJ*, **435**, 66
- Zang, W., Dong, S., Gould, A., et al. 2020, *ApJ*, **897**, 180